Ion irradiation-induced amorphization and nano-crystal formation in garnets

S. Utsunomiya [a], L.M. Wang [a], S. Yudintsev [b], R.C. Ewing [a,c,*]

[a] *Department of Nuclear Engineering and Radiological Sciences, University of Michigan, 1906 Cooley Building, 2355 Bonisteel Boulevard, Ann Arbor, MI 48109-2104, USA*
[b] *Institute of Geology of Ore Deposits, Russian Academy of Sciences, Staromonetny 35, 109017 Moscow, Russia*
[c] *Department of Materials Science and Engineering, University of Michigan, 1906 Cooley Building 2355, Bonisteel Boulevard, Ann Arbor, MI 48109-2104, USA*

Abstract

The radiation susceptibility of garnet structure types ($A_3B_2(XO_4)_3$, I_{a3d}, $Z = 8$) has been examined by 1.0 MeV Kr^{2+} irradiation with in situ transmission electron microscopy over the temperature range of 50–1070 K. The target garnets included five natural garnets: almandine, andradite, pyrope, grossular and spessartine, and five synthetic garnets incorporating various contents of actinides. The synthetic garnets were silicates (N-series) and ferrate–aluminates (G-series). The critical amorphization temperature (T_c), above which amorphization does not occur, were determined to be 1050 K for N77, 1130 K for N56, 1100 K for G3, 890 K for G4 and 1030 K for andradite. T_c of the synthetic garnets increased with increasing mass density of the target and as the electronic-to-nuclear stopping power ratio decreased. During ion irradiation of the G3 garnet at a temperature of 1023 K near the T_c, nano-crystals were produced in which the unit-cell parameter of the original garnet was halved ($\sim$0.64 nm) as a result of a radiation-induced recrystallization process, without evidence for ordering of the cations. © 2002 Elsevier Science B.V. All rights reserved.

1. Introduction

Incorporation of actinides into ceramics is an important issue for the immobilization of actinide-bearing waste streams [1,2]. Garnet is a candidate for the immobilization of HLW because the garnet structure can incorporate actinides, zirconium and rare earth elements. Garnet based ceramics have recently been synthesized for the immobilization of actinide elements [3–6]. Synthetic garnets incorporating rare earth elements are also important for other industrial applications, particularly yttrium aluminum garnet (YAG),

$Y_3Al_5O_{12}$, and YAG doped by other ions for use in laser systems and in digital display systems [7].

The radiation susceptibility of nuclear waste form garnet requires systematic investigation as a function of waste form compositions. Irradiation experiments using heavy ions have been completed for many potential waste form ceramics [8,9], as previous studies have demonstrated that long-term radiation effects due to alpha-decay events may be simulated by the appropriate short-term heavy-ion irradiations [10,11].

Wang et al. [12] first investigated ion-irradiation effects in complex silicates with in situ transmission electron microscopy (TEM). The potential actinide-bearing silicates that have previously been studied by ion-irradiation experiments include zircon, $ZrSiO_4$ [10,13,14]; silicate-apatite, $Ca_{4-x}REE_{6+x}(SiO_4)_{6-y}(PO_4)_yO_2$ [15] and sphene, $CaTi(SiO_4)O$ [16].

Eby et al. [17] have examined the relationship between physical–chemical properties and the critical

* Corresponding author. Address: Department of Nuclear Engineering and Radiological Sciences, University of Michigan, 1906 Cooley Building 2355 Bonisteel Boulevard, Ann Arbor, MI 48109-2104, USA. Tel.: +1-734 647 8529; fax: +1-734 647 8531.

E-mail address: rodewing@umich.edu (R.C. Ewing).

amorphization dose of 25 complex silicates at room temperature. Almandine, andradite, grossular and spessartine garnet were included in the Eby et al. study [17]. However the temperature dependence of the critical amorphization dose of the garnets was not investigated in this first study. A few data for pyrope at $T < 673$ K were measured in a systematic ion irradiation study of phases in the $MgO–Al_2O_3–SiO_2$ system using 1.5 MeV Xe [18]. In this study, ion irradiation (1.0 MeV Kr^{2+}) experiments are completed on five synthetic garnets incorporating different compositions of actinides, Zr, rare earth elements in addition to the five near-end member compositions of natural garnets [19]. Because there are structural similarities between zircon and garnet [20], the results of irradiation in the garnets are also compared with the ion-irradiation experiments of zircon.

The radiation susceptibility of zircon is well studied, because the Zr in zircon can be replaced by Pu [2,21–23]. Zircon shows a two-step dependence of critical dose for amorphization as a function of temperature under 1.5 MeV Kr^+ irradiation; below 300 K and above 475 K [24]. The two-step recovery also has been reported for synthetic zircon [25]. During ion irradiation at elevated temperature ($\sim$970 K), zircon decomposed into nanocrystalline zirconia and amorphous SiO_2, instead of exhibiting a direct crystalline-to-aperiodic transition [26]. Similar to this radiation-induced decomposition, incongruent melting of zircon to constituent oxides

occurs above 1690 °C [27]. Data for long-term (geologic time scale) radiation effects are also available from the study of natural zircon [28,29]. Meldrum et al. [30] have applied ion-irradiation results to the calculation of the degree of radiation damage as a function of uranium content in natural zircon of great age.

2. Garnet structure

The garnet structure has been well studied [31–33], as well as modified structures, e.g., at elevated temperatures [34] or cation-exchanged [35]. Garnet (A_3B_2 $(XO_4)_3$, I_{a3d}, $Z = 8$) is a common structure for orthosilicates. Garnet consists of a distorted cubic close-packed array of oxygens with isometric symmetry. Fig. 1 illustrates the structure of andradite as viewed along the [0 0 1] zone. Six-coordinated BO_6 octahedra and XO_4 tetrahedra establish a framework structure, alternately sharing their corners. The eight-coordinated A-site cation forms AO_8 dodecahedra. Typically, the A-site is occupied by Fe, Ca, Mg or Mn; the B-site, by Fe or Al. Si normally occupies the X-site. Natural garnets are classified into two solid-solution series, grandite and pyralspite. The grandite series includes grossular, $Ca_3Al_2(SiO_4)_3$ and andradite, $Ca_3Fe_2(SiO_4)_3$. The pyralspite series includes pyrope, $Mg_3Al_2(SiO_4)_3$, almandine, $Fe_3Al_2(SiO_4)_3$ and spessartine, $Mn_3Al_2(SiO_4)_3$.
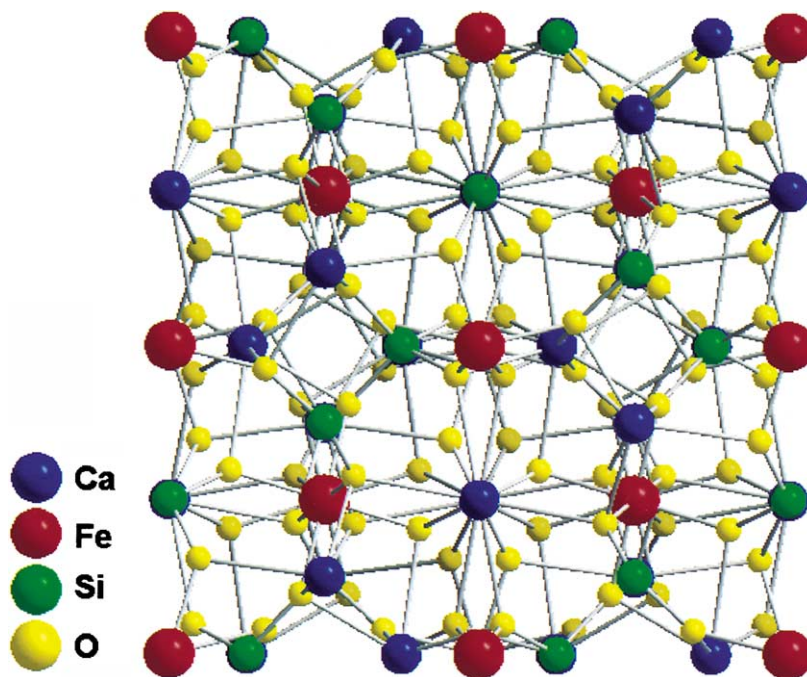

Fig. 1. The structure of andradite along [0 0 1].

For synthetic garnet, both the A-site and B-site can incorporate cations such as actinides depending on the charge balance. The X-site can accommodate Fe^{3+}, Al^{3+}, Ga^{3+}, Ge^{4+} and V^{5+}. These compositions are the ferrates, aluminates, gallates, germinates and vanadates, respectively.

The structure of garnet has a number of important similarities to zircon, $ZrSiO_4$. Zircon ($I4_{1/amd}$, $Z = 4$) consists of an edge-sharing framework of A-site dodecahedra and X-site tetrahedra. Fig. 2 shows the two-dimensional framework of andradite and zircon as viewed along [1 0 0] direction. In this view, the dodecahedra of garnet are considered to be a part of the framework of A-site cations. Both structures show linkages along the directions indicated by the arrows of alternating edge-sharing tetrahedra and dodecahedra. The garnet structure is topologically the same as the structure of zircon after inserting BO_6 octahedra between dodecahedral chains in zircon structure.

3. Experimental

The chemical compositions of the phases in each sample were determined by electron microprobe analysis, EMPA (Cameca, CAMEBAX). The samples were analyzed by a focused beam spot (~5 μm) with a beam current of 20 nA and an accelerating voltage of 20 keV. The Cameca PAP correction routine (modified ZAF) was used for data reduction. Interferences from some overlapping peaks for rare earth elements were checked before the analysis.

Back-scattered electron imaging (BEI) and semi-quantitative anlalyses were performed by field emission scanning electron microscopy (FE-SEM, Philips XL30). TEM and analytical electron microscopy (TEM and AEM, with a JEOL JEM2010F microscope) were used for the initial identification of the phases in each sample. Specimens of materials for TEM were prepared by mechanical polishing to a thickness of a few tens of μm, followed by ion milling using 4.0 keV Ar^+. Before ion-irradiation, all TEM specimens were observed by BEI, and BEI maps were made for all specimens, even for the natural garnets, to ensure the exact position of the garnets in the irradiated section.

All samples were irradiated with in situ TEM observation using 1.0 MeV Kr^{2+} ions in the IVEM (inter-mediate-voltage electron microscope) at the IVEM/HVEM-Tandem Facility of Argonne National Laboratory. The method is the same as described by Wang [9]. According to the result of a SRIM-2000 calculation, the damaged layer caused by 1.0 MeV Kr^{2+} extends to a thickness above 200 nm, so that reliable in situ observation of SAED can be made at the maximum thickness that is penetrated by the electron beam. The dose rate was varied from 12.5×10^{10} to 50×10^{10} ions/cm²/s. The specimen temperature during irradiation varied from 50 to 1073 K. Selected area electron diffraction (SAED) was used to monitor the amorphization process during intervals of increasing irradiation. Subsequent observation was completed by high resolution TEM (HRTEM). The ion dose for complete amorphization, D_c (ions/cm²) was converted to displacements per atom (dpa) and to the kinetic energy transferred to each target atom through nuclear collision (E_n) using SRIM-2000 [36]. These were obtained from the average of damage profile through the sample thickness (~300 nm). In the calculation, the displacement threshold energy, E_d, was assumed to be 23 eV for Si, 47 eV for O and 79 eV for the other cations in the dodecahedral site. These values correspond to the E_d value used in calculations for zircon [37], and 20 eV was used for octahedral cation-site in garnet. Recently, the E_d for individual elements has been
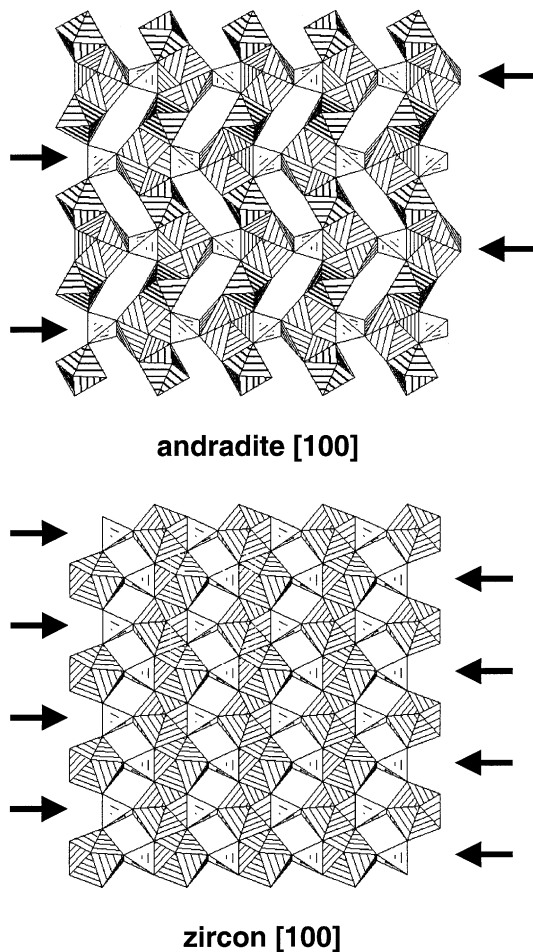

andradite [100]

zircon [100]

Fig. 2. Two-dimensional framework of andradite (a) and zircon (b) along [1 0 0] (10° tilted for zircon to show the edge sharing of polyhedra). The arrows indicate the direction along which similar topological linkages exist.

calculated by molecular-dynamics simulation, and the energies varied depending on the direction of the displacement [38].

The critical amorphization temperature (T_c), above which complete amorphization does not occur, can be obtain by fitting the dose-temperature data based on the model by Weber [10,37,39]. In the model, the relationship between amorphization dose and temperature may be described as follows:

$$\ln\left(1 - \frac{D_0}{D_c}\right) = \ln\left(\frac{1}{\phi\sigma\tau}\right) - \frac{E_a}{kT} \qquad (1)$$

in which D_0 is the amorphization dose at 0 K, D_c is the amorphization dose at temperature, T, ϕ is the ion fluence, σ is the cross-section of cascade damage, τ is the time constant, k is Boltzman's constant. E_a was defined as the activation energy for the dynamic defect annealing process during irradiation in the earlier study [10]. However, the exact meaning of the activation energy is problematic. The kinetic processes controlling amorphization are more complex than the single activated

process as expressed by Eq. (1) [37,39]. A non-linear least squares fitting procedure, without weighting, was used to obtain T_c and E_a in Eq. (1). T_c can be calculated when $D_c = $ infinity, that is the material cannot be amorphized.

4. Results

The back-scattered electron images (BEIs) of the thin sections of the samples, (a) N56, (b) N77, (c) G2, (d) G3 and (e) G4 are shown in Fig. 3(a)–(e). There are several phases in each sample, and major phases are labeled in the figures. The contrast in BEIs corresponds to atomic mass variations; thus, the phase that contains heavier elements shows the brighter contrast. Some samples have many pores, as large as ∼50 μm, and these areas correspond to the black areas in the micrographs.

Chemical compositions by EMPA (the average value of three analytical points) of each phase are given in Table 1. Combined with the EMPA, all phases in the synthetic materials were characterized by SAED and
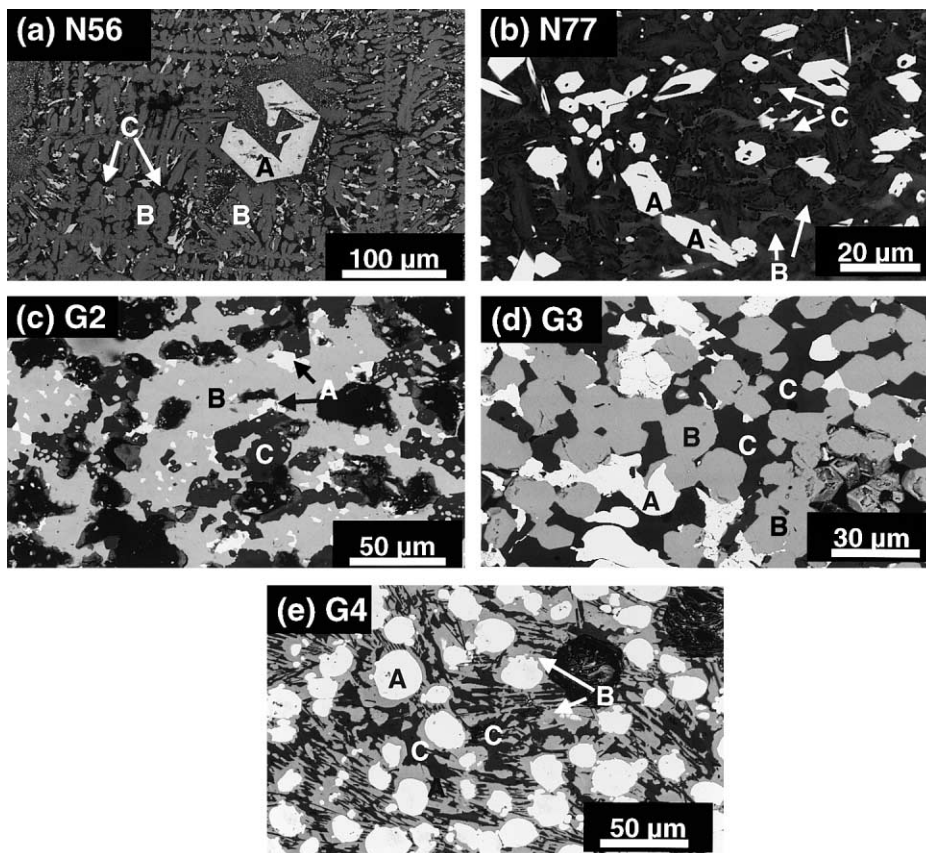

Fig. 3. BEI micrographs of synthetic garnet waste form: (a) N56, (b) N77, (c) G2, (d) G3 and (e) G4. The phases in the micrographic are labeled (A, B and C). Each phase is identified as given in Table 2, and the chemical compositions are given in Table 1 (a).

Table 1
Chemical composition (wt%) of major phases in synthetic garnet-based waste form (Panel A) and of the natural garnets (Panel B) by EMPA

	SiO_2	CaO	La_2O_3	CeO_2	UO_2	ZrO_2	$Fe_2O_3^a$	Nd_2O_3	Eu_2O_3	Gd_2O_3	Al_2O_3
Panel A											
N56 A	20.6	12.0	–	28.7	–	–	1.39	–	–	38.7	–
N56 B	24.5	22.0	–	5.99	–	–	35.2	–	–	11.6	–
N56 C	48.4	42.8	–	1.52	–	–	3.95	–	–	2.33	–
N77 A	21.6	12.3	10.2	19.0	–	3.16	0.84	24.7	7.82	–	–
N77 B	28.7	26.8	0.68	1.25	–	6.80	29.8	2.75	1.19	–	–
N77 C	45.4	18.6	5.67	5.08	–	5.25	11.4	5.03	0.78	–	–
N88 A	23.4	13.7	9.98	16.7	–	6.25	0.73	23.5	5.71	–	–
N88 B1	46.0	24.5	4.15	5.37	–	8.77	0.53	7.96	2.10	–	–
N88 B2	41.1	8.56	4.89	5.00	–	7.45	26.2	5.39	0.93	–	–
N88 C	50.8	44.7	0.20	0.31	–	0.18	1.88	0.67	0.24	–	–
G2A	–	12.8	–	–	74.6	1.51	0.19	–	–	9.35	0.02
G2 B	–	10.1	–	–	3.01	19.7	20.1	–	–	36.1	10.5
G2 C	–	6.33	–	–	0.12	0.76	29.5	–	–	3.49	59.2
G3 A	–	4.84	–	–	53.8	14.7	1.00	–	–	24.6	0.01
G3 B	–	9.43	–	–	2.21	18.4	25.3	–	–	36.9	7.35
G3 C	–	5.80	–	–	0.37	4.33	67.4	–	–	1.32	20.1
G4 A	–	9.93	–	–	23.6	63.8	3.82	–	–	–	0.26
G4 B	–	23.3	–	–	20.5	26.6	20.8	–	–	–	8.49
G4 C	–	14.2	–	–	14.0	0.19	68.9	–	–	–	15.7

	SiO_2	Al_2O_3	$Fe_2O_3^a$	CaO	Cr_2O_3	MnO	MgO
Panel B							
Pyrope	42.6	22.6	10.5	4.29	1.51	0.31	19.5
Spessartine	35.7	20.0	22.4	0.57	0.00	16.7	0.40
Grossular	39.8	19.4	3.25	37.2	0.00	0.00	0.62
Almandine	36.8	20.6	35.2	1.87	0.00	0.77	5.28
Andradite	35.2	0.48	30.1	34.1	0.00	0.00	0.00

[a] All Fe as in Fe_2O_3.

Table 2
The results of phase characterization by FE-SEM, EMPA and AEM

N56	N77	G2	G3	G4
A: britholite	A: britholite	A: calcium uranate	A: calcium uranate	A: $Zr(Ca, U, Fe)O_2$
B: garnet	B: garnet	B: garnet	B: garnet	B: garnet
C: wollastonite	C: amorphous	C: hibonite	C: hibonite	C: calcium–aluminum–ferrite

AEM by referring to the BEI maps. The results of phase characterization are summarized in Table 2. N77 initially contains a small amount of amorphous phase. The natural garnets have impurities, but the andradite has an almost ideal end-member composition. The synthetic garnets in this study are classified into two types: silicate garnet (N series) and ferrate–aluminate garnet (G series). The unit-cell parameters of the synthetic garnets were determined by SAED (Table 3). The **a** cell edge values were 1.25–1.31 nm, which is larger than that of the natural end-member garnets (1.146–1.206 nm).

Table 3
The lattice parameters (nm) of garnets in each sample measured by SAED

N56	N77	G2	G3	G4
1.25	1.27	1.28	1.28	1.31

The radiation-induced transformation of the G3 garnet is shown in the sequence of SAED patterns (Fig. 4). The sequence of SAED patterns reveals that the strong contrast of the defuse halo (amorphous ring)
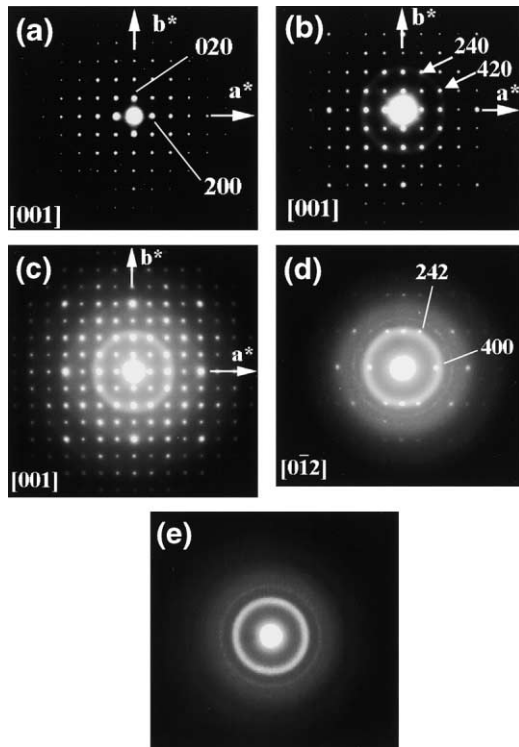
Fig. 4. SAED patterns of G3 garnet irradiated by 1.0 MeV Kr^{2+} at 25 °C: (a) 0 dpa, (b) 0.091 dpa, (c) 0.14 dpa, (d) 0.18 dpa and (e) 0.22 dpa.

appears during irradiation (Fig. 4(b)). The position of the amorphous ring corresponds to a *d*-spacing of 0.286 nm, overlapping 420 and 240.

HRTEM images of G3 garnet during irradiation at room temperature are shown in Fig. 5. Disordered or amorphous domains ($\sim$3 nm) form in the collision cascades that appear in the periodic structure of the garnet (Fig. 5(b)), and the amorphous domains develop by cascade overlap until isolated domains of the crystals remain in an amorphous matrix (Fig. 5(c)) prior to complete amorphization (Fig. 5(d)).

The results of the experiments: critical amorphization dose (D_c), displacement per atom (dpa), the energy loss by nuclear collision (E_n) in the sample at D_c are given in Table 4. The temperature dependences of D_c for the natural garnets (Fig. 6(a)) and of the synthetic garnets (Fig. 6(b)) show a typical behavior, that is an increase in amorphization dose at higher temperatures. Zircon data are plotted in Fig. 6(a) for comparison. There is a two-step temperature dependence of D_c for some natural garnets, as well as the previous data of zircon [26]. In the synthetic garnets, the two-step dependence of D_c could not be recognized clearly except for sample G2, although the synthetic zircon was reported to have a two-step dependence of D_c [25]. In Fig. 6(b), the G2 garnet does

not show a dramatic increase of D_c in the present temperature range (50–1073 K). T_c can be obtained for the synthetic garnets, except for G2: 1100 K for G3, 890 K for G4, 1130 K for N56 and 1050 K for N77. The T_c has a positive correlation with the calculated density by SRIM-2000, which is not a real density but it can be used to compare among the present target materials because the density of the present synthetic garnet is unknown (Table 5). Thus, there is a direct correlation between T_c and the mass of the targets. Activation energies, E_a (eV), were also calculated to be 0.46, 0.35, 0.36 and 0.31, respectively [10]. T_c for natural garnets could not be determined accurately except for andradite because of the lack of data at temperatures above 1073 K (the maximum temperature allowed by the sample holder). However, the garnet compositions can be arranged in order of increasing T_c as follows: pyrope < almandine < grossular < spessartine (close to that of grossular) according to the trend of the D_c–T curves. The order is consistent with the order of the melting points (T_m); pyrope ($\sim$800 °C) < almandine (800 °C) < grossular (850 °C) < andradite (1140 °C) < spessartine (1207 °C) [17], except for andradite. The T_c of andradite was determined to be 1030 K.

In the ion-irradiated G3 garnet at high temperature (near T_c, 1023 K) at a position off-center in the grid, randomly oriented nano-crystals formed that were $\sim$10 nm in size (Fig. 7(b)), although the garnet located at the center of the grid was amorphized. SAED reveals the some sharp rings overlap the original garnet diffraction pattern. The strong contrast ring has the same *d*-spacing as 400 and 040 (the arrow in Fig. 7(a)). This indicates that the nano-crystals have one half the lattice spacing of the original garnet.

5. Discussion

5.1. Comparison with zircon

The average amorphization dose of the natural garnets is 0.21 (dpa) at room temperature. The previously reported dose for zircon is 0.33 (dpa) [24]; thus, the amorphization dose for garnet is less than that of zircon, but of the same order of magnitude at room temperature. The susceptibility of ceramics to amorphization may be evaluated by a consideration of the structural topology [40,41]. The structural freedom parameter, f, which indicates the degree of freedom of the polytopes in assuming new structural arrangement, may be expressed as [42]

$$f = d - C\left\{\delta - \left[\frac{\delta(\delta+1)}{2V}\right]\right\} - (d-1)\frac{Y}{2}$$
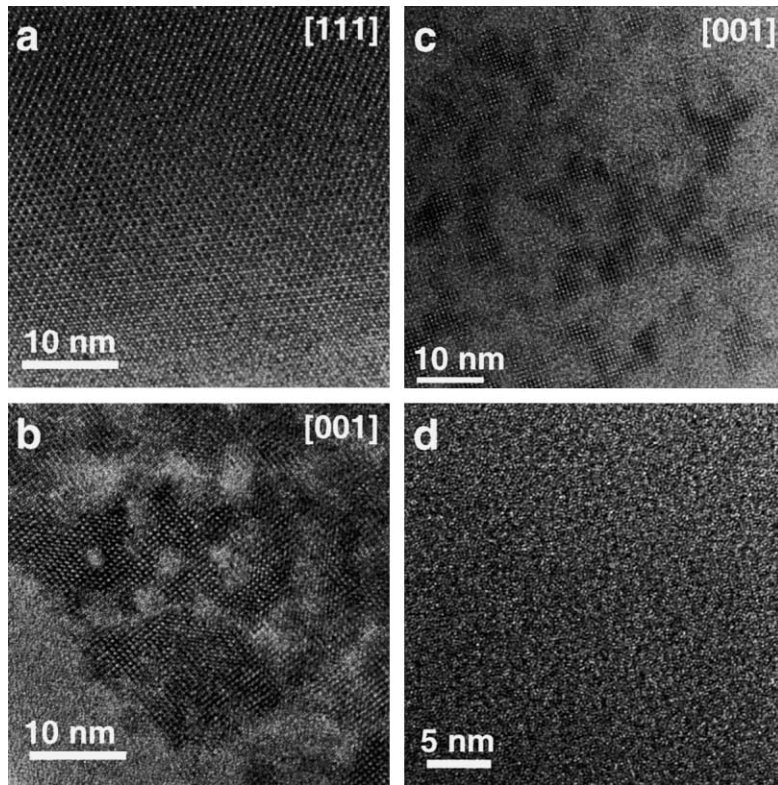$$- [(p-1)d - (2p-3)]\frac{Z}{p}, \qquad (2)$$

Fig. 5. HRTEM image of G3 garnet irradiated by 1.0 MeV Kr^{2+} at 25 °C: (a) 0 dpa, (b) 0.091 dpa, (c) 0.14 dpa and (d) 0.22 dpa.

where d is the dimensionality of the structure, C is the average number of polytopes sharing each vertices, δ is the dimensionality of the constituent polytopes itself, V is the number of vertices in the polytopes, Y is the fraction of edge-sharing vertices, and Z is the fraction of vertices sharing p-sided faces. The structures of garnet and zircon do not have polytopes that share faces; thus, the third term of the equation is eliminated. $\{V, C\}$ is $\{4, 3\}$ for the garnet tetrahedra, $\{6, 3\}$ for the garnet octahedra and $\{4, 3\}$ for zircon tetrahedra. Thus, the structural freedom parameter, f, is calculated to be ~ -2.25 for garnet and ~ -1.5 for zircon. The f-value of garnet is close to that of zircon; thus the topological consideration supports the result that the amorphization susceptibility of garnet is comparable to that of zircon.

The phase diagram of zircon shows the decomposition of zircon to ZrO_2 and SiO_2 above 1690 °C under atmospheric pressure [27]; however, garnets melt congruently at around 1200 °C [34]. A high temperature irradiated zircon also showed decomposition to zirconia and silica [27]; however, garnet does not decompose to amorphous $SiO_2 + MO_x$ during ion irradiation at high temperature. This behavior is consistent with the fact that all of these garnet compositions melt congruently.

The major difference between andradite and the other garnet compositions was the chemical purity. As sug-

gested by a previous study [30], impurities can retard recrystallization and increase T_c. The impurities in the garnets may retard the recrystallization of the disordered zones formed under the ion irradiation.

5.2. The effects of incorporating actinides and REE

The unit-cell parameter of the synthetic garnets varied due to the incorporation of various cations into A-site (Table 3). The change in lattice parameter due to incorporated actinides is similarly observed in zircon [2]. The relationship between the unit-cell parameter and the susceptibility to amorphization cannot be evaluated because of the lower accuracy in measuring the lattice parameter by SAED.

The other factor that affects the susceptibility to amorphization is the atomic mass of the target material. The trend of higher T_c for higher ion mass or mass of the target has been reported in previous ion-irradiation studies on apatite [15], pyrochlore [43] and olivine [44]. The relationship between T_c and mass can be estimated by the nuclear cross-section and maximum transferable kinetic energy to primary knock-on atoms (PKA), such as suggested previously for zircon-structure phosphates, APO_4 [45]. Another parameter that explains the T_c-mass relationship is the ratio of the electronic-to-nuclear

Table 4
Summary of temperature, T (K), the amorphization dose, D_c (10^4 ions/cm^2), the displacement per atom, dpa, and the energy loss by nuclear collision, E_n (eV/atom)

T	D_c	dpa	E_n
almandine			
298	1.81	0.17	15.8
823	4.69	0.44	40.9
943	5.31	0.50	46.3
1023	6.88	0.64	60.0
grossular			
298	1.88	0.16	16.9
823	4.63	0.41	41.6
973	6.88	0.60	61.9
1053	7.25	0.64	65.2
pyrope			
298	2.38	0.20	20.2
823	6.25	0.52	53.1
873	9.06	0.75	77.0
973	12.5	1.0	106
1023	14.4	1.2	122
andradite			
298	1.69	0.18	15.7
573	2.00	0.21	18.6
723	2.50	0.26	23.3
793	2.56	0.27	23.8
873	3.69	0.39	34.4
973	3.44	0.36	32.0
998	9.38	0.98	87.3
1023	17.5	1.8	163
spessartine			
298	3.31	0.32	32.1
823	3.75	0.36	36.3
873	4.06	0.39	39.3
973	4.25	0.40	41.2
1073	4.69	0.45	45.4
N56			
298	1.56	0.18	15.8
773	2.00	0.23	20.2
823	2.13	0.24	21.5
873	2.56	0.29	25.9
973	3.50	0.40	35.4
1053	6.88	0.79	69.5
N77			
298	1.56	0.15	14.0
873	3.19	0.31	28.6
973	7.06	0.70	63.3
G2			
298	1.44	0.21	18.6
823	2.19	0.33	28.3
873	2.25	0.33	29.1
973	2.81	0.42	36.4
1013	3.44	0.51	44.5
1053	3.44	0.51	44.5
1073	3.44	0.51	44.5

Table 4 (*continued*)

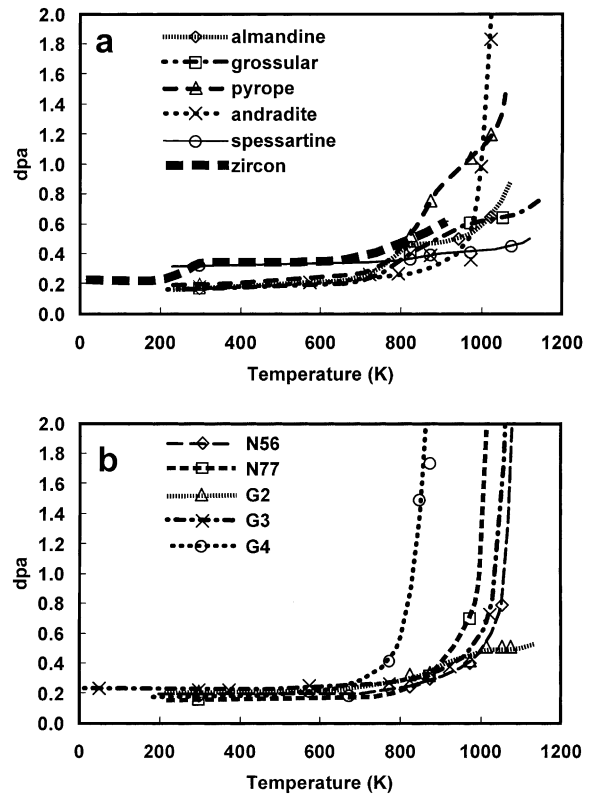| T	D_c	dpa	E_n
G3			
50	1.59	0.23	19.8
298	1.50	0.22	18.7
373	1.53	0.22	19.0
573	1.73	0.25	21.5
773	1.81	0.26	22.5
923	2.59	0.38	32.2
1023	5.00	0.73	62.2
1050	52.5	7.6	653
G4			
298	1.63	0.18	19.5
573	1.88	0.21	22.4
673	1.63	0.18	19.5
773	3.75	0.41	44.8
848	13.6	1.5	162
873	15.8	1.7	189

Fig. 6. Temperature dependence of amorphization dose (dpa) for the natural garnets (a) and the synthetic garnets (b). All targets were irradiated under 1.0 MeV Kr^{2+}.

stopping power (ENSP) [46]. Zinkle [46] and Meldrum et al. [45] proposed the hypothesis that when the ENSP ratio is high, the rate of defect accumulation is low because of high mobility of point defects. The hypothesis is

Table 5
The summary of T_c (K), density (g/cm^3) which is automatically calculated by SRIM-2000, the average electronic (dE/dx_e) and the average nuclear stopping powers (dE/dx_n) calculated using SRIM-2000, and ENSP ratio

	Silicate series			Aluminate–ferrate series		
	N56	N77	Andradite	G2	G3	G4
T_c	1140	1050	1030	–	1100	890
density in SRIM	2.57	2.36	2.22		3.23	3.00
dE/dx_e (eV/atom)	113	113	111		115	116
dE/dx_n (eV/atom)	100	96	92		104	102
ENSP	1.13	1.18	1.21		1.11	1.14
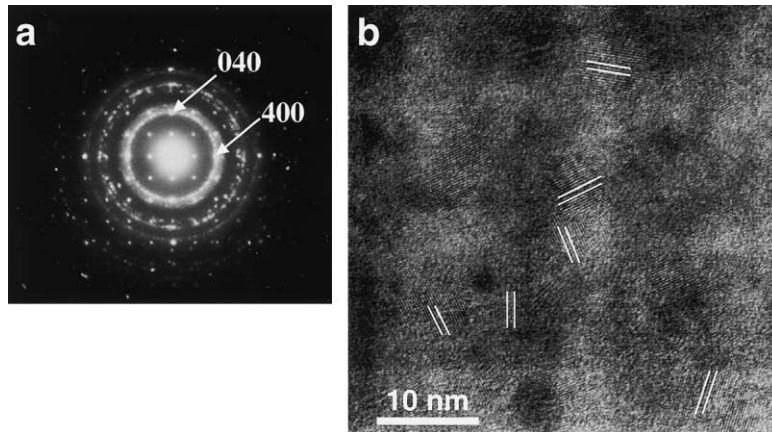
Fig. 7. (a) HRTEM image of G3 garnet irradiated with 1.0 MeV Kr^{2+} at 1023 K. Nano-crystals were produced in a random orientation. The incident beam direction is [1 0 0]. (b) SAED indicates that the nano-crystals have one-half of the d-spacing of the original garnet **a** unit-cell parameter (the arrow).

based on evidence that the dislocation loop density decreases as ENSP ratio increases [46]. In the phosphate case, the hypothesis was successfully applied to explain the fact that the higher T_c has a lower ENSP. Similarly, in the present study, the average nuclear and electron energy loss dE/dx_n and dE/dx_e were calculated by SRIM-2000 for the different targets. The calculated values and ENSP were given with T_c in Table 5. There is a clear trend that T_c increases as ENSP decreases in the both silicate and aluminate–ferrate series. The trend obtained in this study is same as the previously proposed hypothesis [45].

Another parameter that may be correlated to the variation in T_c is the size of the subcascades [43]. The relationship proposed may be expressed as

$$T_c \sim T_m - \frac{(T_m - T_g)R_{cryst}}{rB},$$ (3)

where T_m, T_g, R_{cryst}, r and B are the melting temperature, the glass-transition temperature, the size of the subcascade radius and a constant related to thermal diffusivity, respectively. Although some pa-

rameters are related to the target in addition to the cascade size, T_c has a positive correlation with cascade size. The cascade size can be considered to have a positive correlation to the damage energy per unit volume, which is similar to the nuclear energy loss, dE/dx_n. Although it is not a strong correlation, it is found that T_c increases as the nuclear energy loss increases. This evidence may support the hypothesis that a larger damage energy leads to larger subcascade sizes and to a higher T_c [43].

5.3. Nano-crystal formation

In the G3 garnet, nano-crystals formed at high temperature (1023 K in Fig. 7) at an off-center position on the grid. The temperature distribution in the grid was not homogeneous, and the off-center position may have had a higher temperature than that at the center. Thus, the temperature off-center, where the nano-crystals formed, might be slightly above the actual T_c. Nano-crystals are usually produced when a target is irradiated at a higher temperature [47,48]. According to a recent
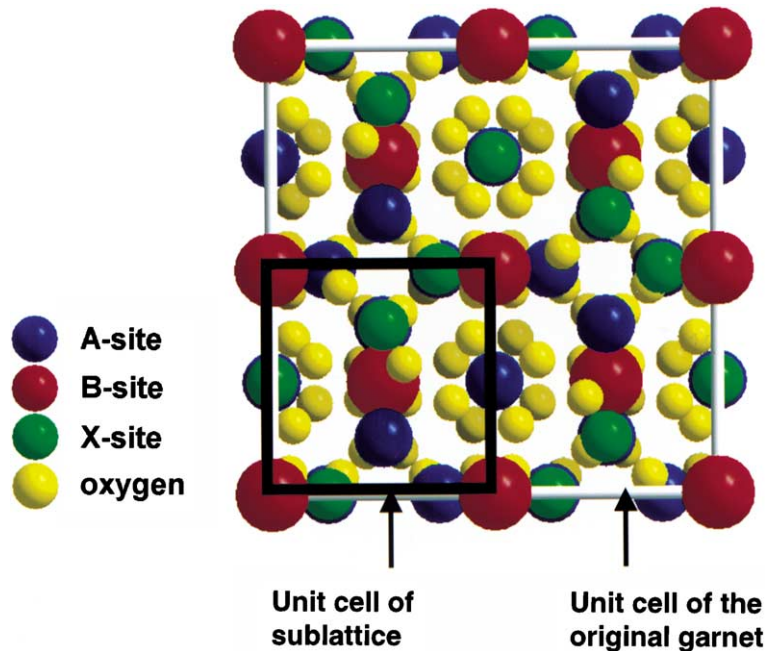
Fig. 8. Schematic cross-sectional view along [0 0 1] of the garnet structure showing the relationship between the garnet structure and the sublattice. A slight relaxation of the oxygen lattice distortion and cation exchange leads to a sublattice with one-half the lattice parameter of the original garnet unit cell.

study on the mechanism of nano-crystal formation [48,49], the ion irradiation-induced nano-crytallization occurs at temperatures near the critical amorphization temperature [50,51], and ion-irradiation induced nano-crystallization results from competition between the formation of amorphous domains and recovery by re-crystallization. During irradiation, some crystalline nuclei may form within the highly disordered zones. When the nuclei exceed a critical size, they become nuclei for recrystallization. This process will depend on the nucleation activation energy and temperature. The randomly oriented nano-crystals form within the amorphous regions if the recrystallization rate for nucleation and growth is high enough.

Various occurrences of radiation-induced nano-crystals have been reported; nano-crystals with the original composition and crystal structure or new nano-phase formed by decomposition of the target material [48–52]. In the case of the synthetic garnet, decomposition did not occur, and the nano-crystals have exactly one-half the lattice spacing of the original garnet unit cell. A similar observation has been made during ion irradiation studies of spinel [44], although nano-crystal formation did not occur. In spinel, the halving of the lattice spacing was attributed to cation disordering. Garnet has a slightly distorted oxygen sublattice. However, when one considers the B-site sublattice, only a slight relaxation of the oxygen distortion and the ex-

change of a few pairs of A-site and X-site cations is required to produce a sublattice with a d-spacing that is one-half of original garnet unit-cell parameter (Fig. 8). Therefore the nano-crystals observed in the synthetic garnets are a cation disordered nano-garnet phase, which is similar to the metastable disordered structure that forms by ion-irradiation of spinel [44,53].

6. Conclusions

Radiation experiments with 1.0 MeV Kr^{2+} were completed in five natural and five synthetic garnets incorporating various compositions of actinides. All of these phases, except for G4, are susceptible to radiation-induced amorphization below 1000 K. T_c of the silicate garnet series, N56, N77 and andradite, are 1130, 1050 and 1030 K, respectively, while the T_c of ferrate–aluminate garnet series, G3 and G4, are 1100 and 890 K, respectively. Both series show a trend of increasing T_c as the ENSP ratio decreases. In addition, T_c is positively correlated to the mass of the target material. At high temperature (1023 K), nano-crystals were produced in ion-irradiated synthetic garnet. These nano-crystals have one-half the lattice spacing of the original garnet structure. The nano-crystals formed due to a radiation-induced recrystallization process, but without the cation ordering characteristic of the garnet structure.

Acknowledgements

References

[1] A.E. Ringwood, S.E. Kesson, N.G. Ware, W. Hibberson, A. Major, Nature 278 (1979) 219.

[2] R.C. Ewing, Proc. Nat. Acad. Sci. USA 96 (1999) 3432.

[3] B.E. Burakov, E.B. Anderson, D.A. Knecht, M.A. Zamoryanskaya, E.E. Strykanova, M.A. Yagovkina, Mater. Res. Soc. Symp. Proc. 556 (1999) 55.

[4] B.E. Burakov, E.B. Anderson, D.A. Knecht, M.A. Zamoryanskaya, M.A. Petrova, Mater. Res. Soc. Symp. Proc. 608 (2000) 419.

[5] S.V. Yudintsev, A Review of LLNL Contract Work. LLNL. UCRL-ID-143846, 2001, p. 295.

[6] S.V. Yudintsev, Proceedings of ICEM'01, 8th International Conference Environment Management, Bruges, Belgium, September 30–October 4, 2001, p. 20.

[7] Y.C. Kang, I.W. Lenggoro, S.B. Park, K. Okuyama, Mater. Res. Bull. 35 (2000) 789.

[8] L.M. Wang, R.C. Ewing, MRS. Bull. 17 (1992) 38.

[9] L.M. Wang, Nucl. Instrum. and Meth. B 141 (1998) 312.

[10] W.J. Weber, R.C. Ewing, L.M. Wang, J. Mater. Res. 9 (1994) 688.

[11] R.C. Ewing, A. Meldrum, L.M. Wang, S.X. Wang, Rev. Miner. Gechem. 39 (2000) 319.

[12] L.M. Wang, R.K. Eby, J. Janeczek, R.C. Ewing, Nucl. Instrum. and Meth. B 59/60 (1991) 395.

[13] A. Meldrum, S.J. Zinkle, L.A. Boatner, R.C. Ewing, Phys. Rev. B 59 (1999) 3981.

[14] A. Meldrum, L.A. Boatner, R.C. Ewing, Mineral. Mag. 64 (2000) 185.

[15] L.M. Wang, W.J. Weber, Philos. Mag. A 79 (1999) 237.

[16] E.R. Vance, F.G. Karioris, L. Cartz, M.S. Wong, in: Proceedings of 2nd International Symposium 85th annual meeting of American Ceramic Society, vol. 8, 1984, p. 64.

[17] R.K. Eby, R.C. Ewing, R.C. Birtcher, J. Mater. Res. 7 (1992) 3080.

[18] S.X. Wang, L.M. Wang, R.C. Ewing, R.H. Doremus, J. Non-Cryst. Solids 238 (1998) 198.

[19] S. Utsunomiya, L.M. Wang, R.C. Ewing, Nucl. Instrum. and Meth. B (2002), in press.

[20] K. Robinson, G.V. Gibbs, P.H. Ribbe, Am. Mineral. 56 (1971) 782.

[21] B.E. Burakov, E.B. Anderson, V.S. Rovsha, S.V. Ushakov, R.C. Ewing, W. Lutze, W.J. Weber, Mater. Res. Soc. Symp. Proc. 412 (1996) 33.

[22] W.J. Weber, R.C. Ewing, W. Lutze, Mater. Res. Soc. Symp. Proc. 412 (1994) 25.

[23] R.C. Ewing, W. Lutze, W. Weber, J. Mater. Res. 10 (1995) 243.

[24] L.M. Wang, R.C. Ewing, W.J. Weber, R.K. Eby, Res. Soc. Symp. Proc. 279 (1993) 451.

[25] W.J. Weber, R. Devanathan, A. Meldrum, L.A. Boatner, R.C. Ewing, L.M. Wang, Mater. Res. Soc. Symp. Proc. 540 (1999) 367.

[26] A. Meldrum, S.J. Zinkle, L.A. Boatner, R.C. Ewing, Nature 395 (1998) 56.

[27] W.C. Butterman, W.R. Foster, Am. Miner. 52 (1967) 880.

[28] H.D. Holland, D. Gottfried, Acta Crystallogr. 8 (1955) 291.

[29] T. Murakami, B.C. Chakoumakos, R.C. Ewing, G.R. Lumpkin, W.J. Weber, Am. Mineral. 76 (1991) 1510.

[30] A. Meldrum, L.A. Boatner, W.J. Weber, R.C. Ewing, Geochim. Cosmochim. Acta 62 (1998) 2509.

[31] S.C. Abrahams, S. Geller, Acta Crystallogr. 11 (1958) 437.

[32] G.V. Gibbs, J.V. Smith, Am. Mineral. 50 (1965) 2023.

[33] G.A. Novak, G.V. Gibbs, Am. Mineral. 56 (1971) 791.

[34] E.P. Meagher, Am. Mineral. 60 (1975) 218.

[35] M.J. Dempsey, Contrib. Mineral. Petrol. 71 (1980) 281.

[36] J.F. Ziegler, J.P. Biersack, U. Littmark, The Stopping and Range of Ions in Solids, Pergamon, New York, 1985.

[37] W.J. Weber, R.C. Ewing, C.R.A. Catlow, T. Diaz de la rubia, L.W. Hobbs, C. Kinoshita, Hj. Matzke, A.T. Motta, M. Nastasi, E.K.H. Salje, E.R. Vance, S.J. Zinkle, J. Mater. Res. 13 (1998) 1434.

[38] B. Park, W.J. Weber, L.R. Corrales, Phys. Rev. B 64 (2001) 174108-1.

[39] W.J. Weber, Nucl. Instrum. and Meth. B 166&167 (2000) 98.

[40] L.W. Hobbs, A.N. Sreeram, C.E. Jesurum, B.A. Berger, Nucl. Instrum. and Meth. B 116 (1996) 18.

[41] L.W. Hobbs, Nucl. Instrum. and Meth. B 91 (1994) 30.

[42] P.K. Gupta, A.R. Cooper, J. Non-Cryst. Solids 123 (1990) 14.

[43] S.X. Wang, L.M. Wang, R.C. Ewing, Phys. Rev. B 63 (2000) 024105-1.

[44] L.M. Wang, W.L. Gong, S.X. Wang, R.C. Ewing, J. Am. Ceram. Soc. 82 (1999) 3321.

[45] A. Meldrum, L.A. Boatner, R.C. Ewing, Phys. Rev. B 56 (1997) 13.

[46] S.J. Zinkle, J. Nucl. Mater. 219 (1995) 113.

[47] A. Meldrum, L.A. Boatner, S.J. Zinkle, S.X. Wang, L.M. Wang, R.C. Ewing, Can. Mineral. 37 (1999) 207.

[48] L.M. Wang, S.X. Wang, R.C. Ewing, A. Meldrum, R.C. Birtcher, B. Newcomer Provencio, W.J. Weber, Hj. Matzke, Mater. Sci. Eng. A 286 (2000) 72.

[49] J. Lian, S.X. Wang, L.M. Wang, R.C. Ewing, J. Nucl. Mater. 297 (2001) 89.

[50] R.C. Birtcher, L.M. Wang, Nucl. Instrum. and Meth. B 59&60 (1991) 966.

[51] L.M. Wang, R.C. Birtcher, R.C. Ewing, Nucl. Instrum. and Meth. B 80 (81) (1993) 1109.

[52] R.C. Birtcher, L.M. Wang, Mater. Res. Soc. Symp. Proc. 235 (1992) 467.

[53] R. Devanathan, N. Yu, K.E. Sickafus, M. Nastasi, J. Nucl. Mater. 232 (1996) 59.